electronics

MDPI

Article

Sub-/Super-SCI Influencing Factors Analysis of VSC-HVDC and PMSG-Wind Farm System by Impedance Bode Criterion

Yibo Zhang, Xu Tian, Cong Wang and Hong Cheng *

School of Mechanical Electronic & Information Engineering, China University of Mining and Technology-Beijing, Beijing 100083, China; bob-yibo.zhang@student.cumtb.edu.cn (Y.Z.); tianxu516@163.com (X.T.); wangc@cumtb.edu.cn (C.W.)

* Correspondence: chengh@cumtb.edu.cn

Abstract: A sub-/super-synchronous interaction (sub-/super-SCI) can occur between a voltage source converter-based high-voltage direct current (VSC-HVDC) and the permanent magnet synchronous generator (PMSG)-based wind farms with long AC transmission lines. However, the influencing factors have not been properly analyzed. In this paper, these are deconstructed and mathematically analyzed from detailed small-signal impedance equations in the *dq*-frame and the corresponding Bode stability criterion. Distinguishing conclusions from existing papers are obtained by studying the controllers' bandwidths instead of their coefficients. The impacts of AC line impedance on system stability are also investigated. From the analysis of their compositions in impedance structure, the VSC-HVDC bandwidths and the wind farm phase-locked loop (PLL) bandwidth and power ratio, and the AC line impedance have various influences on the system stability. Meanwhile, the wind farm outer DC voltage and inner current control bandwidths have little impact on system stability. The results of these studies show that the magnitude in the axes *q-axes* impedance interaction is the essential factor for system instability. Our studies also show system stability is more sensitive to the HVDC bandwidths than the wind converter PLL bandwidth. The simulation results verify our theory conclusions.

Keywords: impedance; VSC-HVDC; PMSG-wind farm; sup/sub-SCI; stability; bandwidth; line impedance

check for updates

Citation: Zhang, Y.; Tian, X.; Wang, C.; Cheng, H. Sub-/Super-SCI Influencing Factors Analysis of VSC-HVDC and PMSG-Wind Farm System by Impedance Bode Criterion. *Electronics* **2021**, *10*, 1865. https://doi.org/10.3390/electronics10151865

Academic Editor: Hani Vahedi

Received: 5 July 2021
Accepted: 29 July 2021
Published: 3 August 2021

Publisher's Note: MDPI stays neutral with regard to jurisdictional claims in published maps and institutional affiliations.

Copyright: © 2021 by the authors. Licensee MDPI, Basel, Switzerland. This article is an open access article distributed under the terms and conditions of the Creative Commons Attribution (CC BY) license (https://creativecommons.org/licenses/by/4.0/).

1. Introduction

In response to the development of large-scale onshore and offshore wind farms, PMSG wind turbines have been gaining popularity for their ease of maintenance and dynamic performance in grid voltage fault ride through [1]. In addition to being used for long-distance power transmission, HVDC is becoming increasingly popular for its economic advantages [2]. Due to the requirement for HVDC as a voltage source mode in the HVDC-based wind farm dedicated transmission line system, VSC-HVDC plays a prominent role in this application scenario. It is available in two-level [3], multilevel, and modular multilevel converter types [4]. Power electronics converters make up this system, which lacks the inertia offered by strong grids and synchronized generators [5]. As a result, sub-synchronous oscillations and super-synchronous oscillations pose a challenge. These oscillations are multi-frequency and time-varying [6]. The mechanism of these oscillations, unlike conventional power systems which comes from passive inducive and capacitive, needs to be explained by new methods [7].

The first case of sub-synchronous oscillations occurred in Texas, USA, in 2009. Paper [8] yields these by means of controlled interactions for the first time. The first case of sub-synchronous oscillations in China in 2012 was studied by paper [9]. Researchers have conducted many works and studies after these cases. In paper [10], the mechanisms of low frequency oscillation in the VSC-HVDC with doubly fed induction generator (DFIG)

wind farm system was investigated. The system instability was due to the negative damping brought about by phase-locked loop (PLL) in RLC equivalent models. Paper [11] demonstrated the role of the rotor-side converter (RSC) in low frequency oscillation in the VSC-HVDC with DFIG wind farm system. In paper [12,13], low frequency oscillation current components at the positive and negative sequence were analyzed. The frequency relationship between low frequency oscillation current components and rotor side current and DC side voltage was revealed. However, all these articles concern the DFIG wind farm. Paper [14] presents a PMSG based wind farm and VSC-HVDC sequence impedance model by the harmonic linearization method. Paper [15] focuses on the impact of different power converter models' application on the VSC-HVDC with PMSG wind farm. In paper [16], circulating current control of the VSC-HVDC system was studied as a significant effect on the stability of the VSC-HVDC with PMSG wind farm system. Paper [17] built a *dq*-frame-based impedance models. These papers indicate that the mechanism of sup/sub-SCI is the interaction between the controls of the VSC-HVDC and controls of the wind farm. However, all these papers lack a study of system stability influencing factors. Analysis of controller parameters in [18,19] showed that increasing control proportion of the wind farm's inner current control loop could increase system instability risk. Nonetheless, these papers examined each controller's coefficient individually, without introducing concepts based on closed-loop models for bandwidth. Moreover, our research has different conclusions from these two papers when studying the impacts of the PMSG wind converter current control loop bandwidth instead of its controller. Paper [20] also investigated the impact of controllers of the VSC-HVDC and PMSG-based wind farm on system instability. However, this paper focuses on damping methods to suppress the oscillation. The paper [21] analyzed the impact of power ratio and controllers on system stability. However, it was not explained in terms of impedance structure and mathematics, which gave insufficient understanding of the root causes of the influence. Furthermore, the existing literature still lacks VSC-HVDC impedance models which consider the filter capacitor current control, thus reducing the accuracy of VSC-HVDC impedance models. Moreover, the general Nyquist criterion (GNC) application in these papers considers the unstable conditions of both *d-axes* and *q-axes* impedance together. This limits system instability factors' analysis from phase and magnitude aspects in *d-axes* and *q-axes* separately. Consequently, existing research has failed to provide an in-depth analysis of the influencing factors on supra/sub-SCI, that would take into account the tuning process of the real controllers and the AC line impedance, and mathematically evaluate the role the influences play in impedance structures.

This paper investigates a dedicated wind farm transmission line system, in which a PMSG-based wind farm transmits power to the main AC grid through a two-level VSC-HVDC. Small signal models in *dq*-frame are built and an impedance-based bode criterion is introduced. Impedance on the *q-axes* is an essential element for stable criterion due to its impedance characteristics. Low frequency interactions between wind farm impedance and HVDC sending terminal impedance could lead to oscillations.

Compared to existing studies, the contributions of this paper are as following:

(1) Detailed analytical expressions of *d-axes* and *q-axes* impedance of PMSG wind farm and VSC-HVDC are present. These expressions contain all possible influencing factors on system stability, such as wind farm power ratios (current), AC line impedance, and controllers' parameters. Compared with formatting the impedance expressions in matrix form, as seen in existing surveys, the detailed analytical expressions are more conducive to analysis of the influencing factors' impacts, both structurally and mathematically.

(2) Compared with existing papers, this paper gives a study of the controllers impacts on system stability from the perspective of bandwidth. Impedance equations are reconstructed for their contained bandwidths. To follow the tuning process of PI controllers' processes, the proportional relationship of inner and outer control bandwidths is kept. By varying the bandwidths, their impacts and sensitivity are identified. The

reasons why the different bandwidths affect system stability in markedly different ways are explained.

(3) A method of enhancing system stability using bandwidth modification is also discussed in this paper. Based on the acceptable range, the more sensitive factors are selected for the shaping of the impedance for system stability improvement.

The rest of this paper is organized as follows: Section 2 gives a small signal impedance model of the system controllers in the *dq*-frame, including the PMSG-based wind farm and VSC-HVDC sending terminal. Section 3 presents the impedance-based system stability analysis. Power ratio, line impedance, and the bandwidths of all controllers are theoretically analyzed using detailed impedance expressions and the Bode criterion. In Section 4, simulation results and stability improvements by bandwidth adjustments and their sensitivities are presented. Finally, Section 5 presents the conclusions and discussion.

2. VSC-HVDC Sending Terminal and PSMG-Wind Farm Impedance Modeling

2.1. System Description

Figure 1 introduces a PMSG-based wind farm with a two terminal VSC-based HVDC system. The wind power grid side converter works as an AC current source, which is connected to the point of common coupling (PCC) through a transformer and AC transmission line. The HVDC sending terminal works as an AC voltage source to support the PCC. The HVDC receiving terminal is connected to the main power grid by a transformer. To simplify this system, the wind power generator side converters are considered as a DC current source, and a DC-link of HVDC is a constant DC voltage source. Consequently, for wind farms, only DC-link and grid side converters will be modelled. Meanwhile, the HVDC receiving terminal and the main power grid will be neglected in the following analysis.

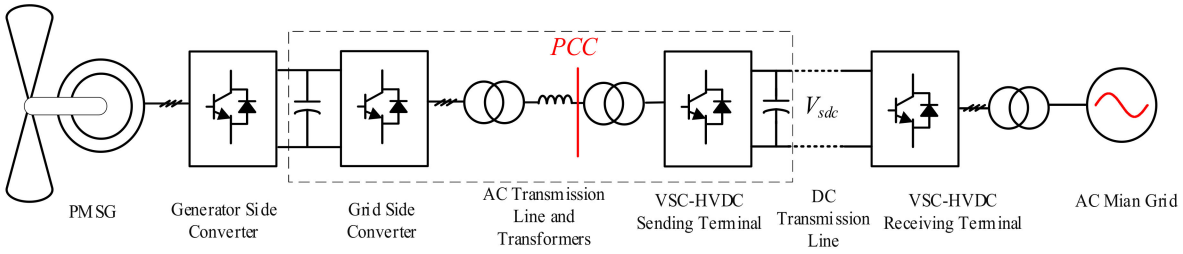

Figure 1. Schematic diagram of PMSG-based wind farm and VSC-HVDC system.

2.2. VSC-HVDC Sending Terminal Control Bandwidths

Figure 2 shows the HVDC schematic circuit. The inductance, resistance and capacitance of the HVDC sending terminal converter *LC* filter are given by R_s, L_s and C_s, where the subscript '*s*' denotes the HVDC sending terminal. The equivalent inductance of the transformer is given by L_{st}, and V_{sdc} represents the HVDC DC-link equivalent voltage. The valve voltage of the converter U_s is considered as an ideal controllable three-phase voltage source.

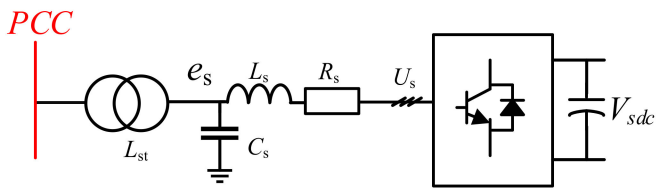

Figure 2. VSC-HVDC sending terminal schematic circuit.

All models in this paper were built in a dq synchronization reference frame to correspond to the normal PI controller application in the converter. For a HVDC sending

terminal, the *d-axes* aligned with the voltage vector e_s (the C_s voltage), and the *q-axes* leads the *d-axes* by $\pi/2$.

Figure 3 shows the dual-loop control loop schematic diagram of the HVDC sending terminal [22], where e_{sd}, e_{sq}, u_{sd}, u_{sq} are the C_s voltage and HVDC converter valve side voltages in the *dq*-frame, denoted by the subscript 'd' and 'q', respectively. The corresponding L_s currents are i_{sLd} and i_{sLq}.

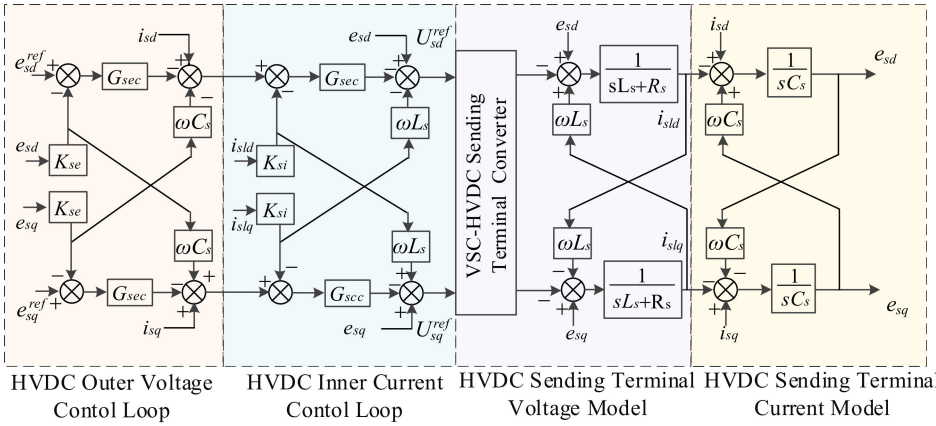

Figure 3. VSC-HVDC sending terminal control schematic.

A closed-current control loop C_{scc} is given in Equation (1), which describes the current dynamic performance in both the d and q-axes. The transfer function of the current controller is given by $G_{scc} = k_{spcc} + k_{sicc}/s$.

$$C_{scc} = \frac{sk_{spcc} + k_{sicc}}{s^2 L_s + s\left(R_s + k_{spcc}\right) + k_{sicc}} \tag{1}$$

Equation (1) is modified to a first-order form by setting $k_{spcc} = \omega_{scc} L_s$ and $k_{sicc} = \omega_{scc} R_s$ as Equation (2), where ω_{scc} is the bandwidth of the closed current loop.

$$T_{scc} = \frac{\omega_{scc}}{s + \omega_{scc}} \tag{2}$$

A closed AC voltage control loop can be expressed as Equation (3), where $G_{sec} = k_{spec} + k_{siec}/s$ is the AC voltage PI controller.

$$C_{sec} = \frac{sk_{spec} + k_{siec}}{s^2 C_s + sk_{spec} + k_{siec}} \tag{3}$$

The closed-loop is written in a second-order form as Equation (4) by letting $k_{spec} = 2\varsigma_{sec}\omega_{snec} C_s$ and $k_{siec} = \omega_{snec}^2 C_s$, where ς_{sec} is the damping of the voltage control loop, and ω_{snec} is its natural frequency.

$$T_{sec} = \frac{2\varsigma_{sec}\omega_{snec} + \omega_{snec}^2}{s^2 + 2\varsigma_{sec}\omega_{snec} + \omega_{snec}^2} \tag{4}$$

Defining the AC voltage closed-loop bandwidth ω_{sec} when $|T_{sec}| = 0.707$, the relationship between the bandwidth ω_{sec} and the natural frequency ω_{snec} can be calculated using Equation (5).

$$\omega_{snec} = \omega_{sec}\left(\left(4\varsigma_{sec}^4 + 4\varsigma_{sec}^2 + 2\right)^{\frac{1}{2}} - 2\varsigma_{sec}^2 - 1\right)^2 \tag{5}$$

2.3. VSC-HVDC Sending Terminal Impedance Modeling

To build the impedance model, the expression of a matrix form **ΔU = ZΔI** should be calculated [12], where **Z** is a 2 × 2 matrix impedance, and **ΔU** and **ΔI** are small signal voltage and current matrices of size 2 × 1 in the *dq*-frame. The bold letters represent matrix in this paper.

The VSC-HVDC sending terminal impedance in the *dq*-frame can be written as $\mathbf{Z_{s0}}$, which is given as follows in Equation (6):

$$\mathbf{Z_{s0}} = \begin{array}{c} ((\mathbf{I}-\mathbf{G_{sdel}}(\mathbf{I}-\mathbf{G_{scc}}\mathbf{G_{sec}}+\mathbf{G_{scc}}\mathbf{G_{sdee}}))+(\mathbf{G_{sdel}}(\mathbf{G_{sdec}}-\mathbf{G_{scc}})+\mathbf{Z_{sL}})\mathbf{Y_{sc}})^{-1} \\ (\mathbf{G_{sdec}}\mathbf{G_{sdel}}+\mathbf{Z_{sL}}) \end{array} \quad (6)$$

where

$$\mathbf{Z_{sL}} = \begin{bmatrix} sL_s + R_s & -\omega L_s \\ \omega L_s & sL_s + R_s \end{bmatrix}, \mathbf{Y_{sc}} = \begin{bmatrix} sC_s & -\omega C_s \\ \omega C_s & sC_s \end{bmatrix}, \mathbf{G_{sec}} = -\begin{bmatrix} G_{\text{sec}} & 0 \\ 0 & G_{\text{sec}} \end{bmatrix}$$

$$\mathbf{G_{scc}} = -\begin{bmatrix} G_{scc} & 0 \\ 0 & G_{scc} \end{bmatrix}, \mathbf{G_{sdee}} = -\begin{bmatrix} 0 & -\omega C_s \\ \omega C_s & 0 \end{bmatrix}, \mathbf{G_{sdec}} = -\begin{bmatrix} 0 & -\omega L_s \\ \omega L_s & 0 \end{bmatrix}$$

2.4. PMSG-Wind Converter Control Bandwidths

A type IV wind turbine with L filter connected to the PCC through a transformer and a cable is shown in Figure 4. An ideal converter model is used regardless of the PWM harmonic effect.

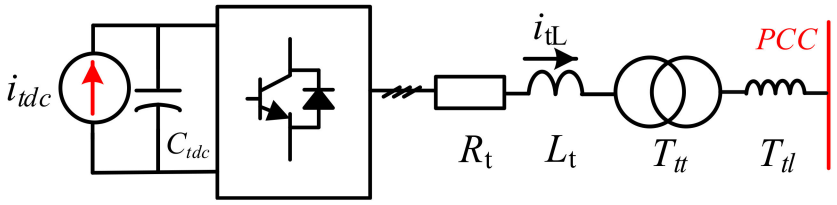

Figure 4. PMSG-based wind system equivalent schematic circuit.

Figure 5 shows the outer DC-link voltage and inner current control loop schematic diagram of the grid side converter. The subscript 't' stands for the wind turbine.

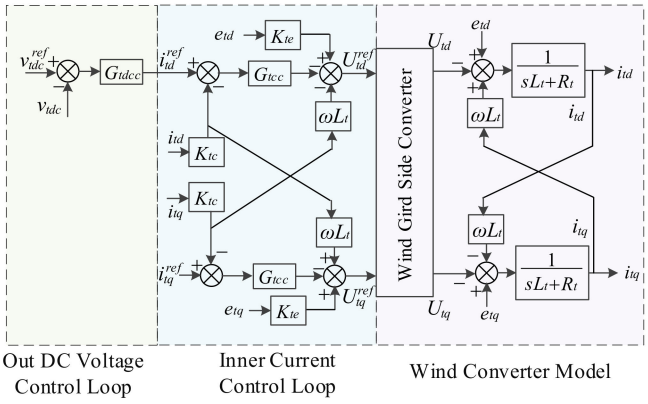

Figure 5. PMSG-based wind converter control schematic.

A current closed-loop in the d and q-axes can be obtained with Equation (7), where $G_{tcc} = k_{tpcc} + k_{ticc}/s$ is the current PI controller, and L_t and R_t are the inductor and resistance of L filter, respectively.

$$C_{tcc} = \frac{sk_{tpcc} + k_{ticc}}{s^2 L_t + s(R_t + k_{tpcc}) + k_{ticc}} \quad (7)$$

Equation (7) can be modified as a typical first-order transfer function as Equation (8) by $k_{tpcc} = \omega_{tcc}L_t$ and $k_{ticc} = \omega_{tcc}R_t$, where ω_{tcc} is the bandwidth of the closed current loop.

$$T_{tcc} = \frac{\omega_{tcc}}{s + \omega_{tcc}} \tag{8}$$

The DC-link voltage closed-loop is given by Equation (9), where $G_{tdcc} = k_{tpdcc} + k_{tidcc}/s$ is the DC-link voltage PI controller, and C_{tdc} is the DC-link capacitor. Setting $k_{tpdcc} = 2\varsigma_{tdcc}\omega_{tndcc}C_{tdc}$ and $k_{tidcc} = \omega_{tndcc}^2 C_{tdc}$, Equation (9) can be modified as a typical second-order transfer function through Equation (10), where the damping ratio and natural frequency are given by ς_{tdcc} and ω_{tndcc}, respectively. Introducing the DC-link voltage closed loop bandwidth ω_{tdcc} which makes $|T_{tdcc}| = 0.707$, Equation (11) give the relationship between ω_{tndcc} and ω_{tdcc}.

$$C_{tdcc} = \frac{\frac{k_{tpdcc}}{C_{tdc}}s + \frac{k_{tidcc}}{C_{tdc}}}{s^2 + \frac{k_{tpdcc}}{C_{tdc}}s + \frac{k_{tidcc}}{C_{tdc}}} \tag{9}$$

$$T_{tdcc} = \frac{2\varsigma_{tdcc}\omega_{tndcc} + \omega_{tdcc}^2}{s^2 + 2\varsigma_{tdcc}\omega_{tndcc} + \omega_{tndcc}^2} \tag{10}$$

$$\omega_{tnecc} = \omega_{tdcc}\left(\left(4\varsigma_{tdcc}^4 + 4\varsigma_{tdcc}^2 + 2\right)^{\frac{1}{2}} - 2\varsigma_{tdcc}^2 - 1\right)^2 \tag{11}$$

Figure 6 illustrates the block diagram of a common PLL, where the three-phase grid voltage e_{abc} is needed as the input, and the grid voltage phase θ is the output.

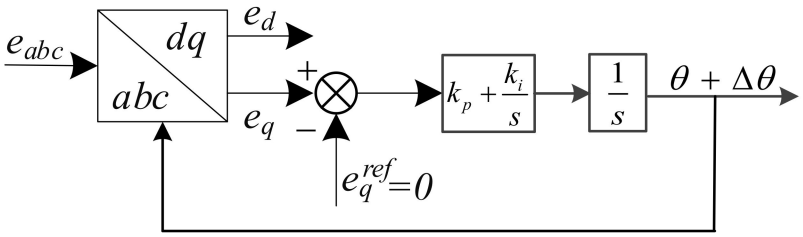

Figure 6. PMSG-based wind system equivalent schematic current.

From paper [23], the closed PLL control loop is given as Equation (12), where $G_{tpllc} = k_{tppll} + k_{tipll}/s$ is a PLL PI controller, and e_{tx} is the grid voltage without perturbation.

$$G_{tpll} = \frac{G_{tpllc}}{s + e_{tx}G_{tpllc}} \tag{12}$$

The closed PLL control loop can be re-expressed as T_{tpll} by setting $k_{tppll} = 2\varsigma_{tpllc}\omega_{tnpll}/e_{td}$ and $k_{tppll} = \omega_{tnpll}^2/e_{tx}$.

$$T_{tpll} = \frac{1}{e_{tx}}\frac{2\varsigma_{tpll}\omega_{tnpll} + \omega_{tnpll}^2}{s^2 + 2\varsigma_{tpll}\omega_{tnpll} + \omega_{tnpll}^2} \tag{13}$$

By defining the bandwidth when $|T_{tpll}| = 0.707$, the relationship between the PLL bandwidth and the natural frequency is shown by Equation (14).

$$\omega_{tnpll} = \omega_{tpll}\left(\left(4\varsigma_{tpll}^4 + 4\varsigma_{tpll}^2 + 2\right)^{\frac{1}{2}} - 2\varsigma_{tpll}^2 - 1\right)^2 \tag{14}$$

2.5. PMSG-Wind Converter Impedance

Based on the outer DC-link voltage control loop and the inner current and PLL control loops, the impedance of the PMSG wind grid side converter can be derived from Equation (15); the detailed impedance-built process can be found in paper [24]. The subscript '*x*'

and 'y' stands for the system frame x-axes and y-axes, which are defined as the same as dq-frame when there is no perturbance in grid voltage. e_{tx} and e_{ty} and i_{tx} and i_{ty} are the grid side voltage and current in x-axes and y-axes.

$$\mathbf{Z_{t0}}= \begin{array}{c} \left(\mathbf{Z_{tL}}-\mathbf{G_{tdel}}\left(\mathbf{G_{tdec}}-\mathbf{G_{tcc}}-\mathbf{G_{tcc}}\mathbf{G_{tdcc}}\mathbf{G^{i}_{tdc}}\right)\right)^{-1} \\ \left(\mathbf{I}\text{-}\mathbf{G_{tdel}}\mathbf{G^{u}_{tpll}}\mathbf{K_{te}}\text{-}\mathbf{G_{tel}}\mathbf{K_{te}}\left(\mathbf{G^{e}_{tpll}}+\mathbf{G_{tdec}}\mathbf{G^{i}_{tpll}}\text{-}\mathbf{G_{tcc}}\mathbf{G^{i}_{tpll}}\text{-}\mathbf{G_{tcc}}\mathbf{G_{tdcc}}\mathbf{G^{e}_{tdc}}\right)\right) \end{array} \tag{15}$$

where

$$\mathbf{Z_{tL}} = \begin{bmatrix} sL_t + R_t & -\omega L_t \\ \omega L_t & sL_t + R_t \end{bmatrix}, \mathbf{G^{e}_{tdc}} = \frac{1}{sC_t v_{dc}} \begin{bmatrix} i_{tx} & i_{ty} \\ 0 & 0 \end{bmatrix}, \mathbf{G^{i}_{tdc}} = \frac{1}{sC_t v_{dc}} \begin{bmatrix} e_{tx} & e_{ty} \\ 0 & 0 \end{bmatrix}$$
$$\mathbf{G^{e}_{tpll}} = \begin{bmatrix} 1 & e_{ty}G_{tpll} \\ 0 & 1 - e_{tx}G_{tpll} \end{bmatrix}, \mathbf{G^{i}_{tpll}} = \begin{bmatrix} 0 & i_{ty}G_{tpll} \\ 0 & -i_{tx}G_{tpll} \end{bmatrix}, \mathbf{G^{u}_{tpll}} = \begin{bmatrix} 0 & -u_{tq}G_{tpll} \\ 0 & -u_{td}G_{tpll} \end{bmatrix}$$
$$\mathbf{G_{tcc}} = -\begin{bmatrix} G_{tcc} & 0 \\ 0 & G_{tcc} \end{bmatrix}, \mathbf{G_{tdcc}} = -\begin{bmatrix} G_{tdcc} & 0 \\ 0 & 0 \end{bmatrix}, \mathbf{G_{tdec}} = -\begin{bmatrix} 0 & -\omega L_t \\ \omega L_t & 0 \end{bmatrix}$$

3. Impedance-Based System Stability Analysis

3.1. Basic Theory of the Impedance-Based System Stability Criterion

To employ the impedance stability criterion, the wind farm system with HVDC is divided into two interconnected parts by the PCC as shown in Figure 7. The impedance of the HVDC sending terminal is given by $\mathbf{Z_s}$ and its transformer impedance is $\mathbf{Z_{st}}$. Meanwhile, $\mathbf{Z_t}$ contains the impedance of the remaining parts that include wind grid side converters, step up transformer's impedance $\mathbf{Z_{tt}}$ and AC transmission line impedance $\mathbf{Z_{tl}}$. The expressions $\mathbf{Z_s}$ and $\mathbf{Z_t}$ are given by Equations (16) and (17), respectively.

$$\mathbf{Z_s} = N_{st}^2(\mathbf{Z_{s0}}+\mathbf{Z_{st}}) \tag{16}$$

$$\mathbf{Z}_t = \frac{N_{tt}^2}{N_t^2}(\mathbf{Z_{t0}}+\mathbf{Z_{tt}}) + \mathbf{Z_{tl}} \tag{17}$$

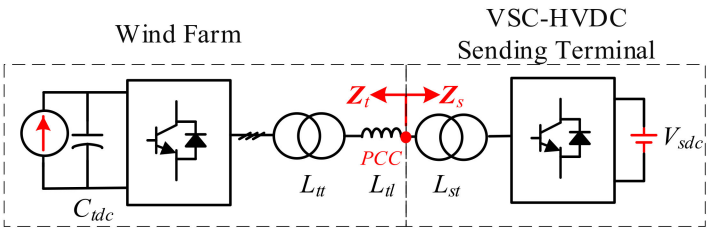

Figure 7. PMSG-wind farm with VSC-HVDC system impedance division.

The transformer ratios of the HVDC and wind converter sides are given by N_{st} and N_{tt}, respectively. N_t is the number of grid-connected wind power grid side converters.

$$\mathbf{Z_{st}} = \begin{bmatrix} sL_{st} & -\omega L_{st} \\ \omega L_{st} & sL_{st} \end{bmatrix}, \mathbf{Z_{tt}} = \begin{bmatrix} sL_{tt} & -\omega L_{tt} \\ \omega L_{tt} & sL_{tt} \end{bmatrix}, \mathbf{Z_{tl}} = \begin{bmatrix} sL_{tl} & -\omega L_{tl} \\ \omega L_{tl} & sL_{tl} \end{bmatrix}$$

Both $\mathbf{Z_s}$ and $\mathbf{Z_t}$ are size 2×2 matrices, and the GNC can be used for system stability analysis. The minor loop gain of the equal feedback control system is given as:

$$\mathbf{G(s)H(s)}=\frac{\mathbf{Z_t}}{\mathbf{Z_s}}$$

which is also a 2×2 matrix. The minor loop gain matrix is defined as:

$$\mathbf{G(s)H(s)}=\begin{bmatrix} Z_{dd} & Z_{dq} \\ Z_{qd} & Z_{qq} \end{bmatrix}$$

Generally, **G(s)H(s)** is asymptotically stable if and only if the characteristic loci for the eigenvalues of **G(s)H(s)**, $\lambda_1(s)$ and $\lambda_2(s)$ taken together, do not encircle -1 for $s = j\omega$, and $-\infty < \omega < \infty$ [21], where:

$$\lambda_{1,2}(s) = \frac{Z_{dd} + Z_{qq}}{2} \pm \sqrt{\left(\frac{Z_{dd} - Z_{qq}}{2}\right)^2 - Z_{dq}Z_{qd}}$$

If the off-diagonal elements Z_{dq} and Z_{qd} are relatively low in gain compared with the diagonal elements Z_{dd} and Z_{qq}, the eigenvalues of **G(s)H(s)** can be simplified to an approximate form with negligible impact on the system stability analysis [25,26].

$$\lambda_{1,2}(s) = Z_{dd}, Z_{qq}$$

Because the Bode plots of Z_{dd} and Z_{qq} correspond to their Nyquist plot, the Bode criterion has the same function as the GNC, which will be explained later. Furthermore, the bode criterion can be used to easily observe individual magnitude and phase stability tendency. Therefore, the Bode criterion is used as the main system stability criterion.

Additionally, before using the impedance stability criterion, the two parts from the PPC shown in Figure 7 should be individually stable. This requires the HVDC sending terminal to be stable when unloaded due to its voltage source working mode. Meanwhile, the wind power converter should be kept stable when connected to an ideal voltage source due to its current source working mode. All the cases in this study satisfied these two conditions.

3.2. Impedance Characters Analysis and Impact of Power Ratio on System Stability

To analyze the sub-/super-synchronous phenomenon by using the impedance criterion, detailed expression of $\mathbf{Z_s}$ and $\mathbf{Z_t}$ should be formulated. To apply the unity power factor control to wind power converters, the voltage and current in the *q-axes* are all considered to be equal to zero in the stable state. In addition, the wind grid side converter valve side voltage u_{td} and u_{tq} can be replaced by the grid voltage and current in the *d-axes* as $u_{td} = e_{td} - R_t i_{td}$ and $u_{tq} = -\omega L_t i_{td}$ in the expression for the wind farm impedance in Equation (17). The off-diagonal elements in Equation (17) can also be neglected due to the unity power factor control [17,27,28]. Therefore, the minor loop gain can be simplified to an approximate form as $\lambda_1(s) = Z_{sdd}/Z_{tdd}$ and $\lambda_2(s) = Z_{sqq}/Z_{tqq}$. The PWM delay and the voltage and current sample delays can also be neglected due to their small impact on the frequency band this paper is concerned with.

Based on the above conditions, the diagonal element expressions are given in Equations (18)–(20), where Z_{sdd} and Z_{sqq} represent HVDC sending terminal impedance on *d* and *q-axes*, respectively, Z_{tdd} and Z_{tqq} are the wind farm impedance in the *d* and *q-axes*, respectively.

$$Z_{sdd,sqq} = \frac{N_{st}^2 \frac{G_{scc}G_{\sec} + (G_{scc} + sL_s + R_s)sC_s}{sL_s + R_s}}{\left(\frac{G_{scc}G_{\sec} + (G_{scc} + sL_s + R_s)sC_s}{sL_s + R_s}\right)^2 + (\omega C_s)^2} + sL_{st} \tag{18}$$

$$Z_{tdd} = \frac{N_{tt}^2}{N_t}\left(\frac{sL_t + R_t + G_{tcc}}{G_{tcc}G_{tdcc}}\right)\frac{sC_{tdc}v_{tdc}}{i_{td}} - \frac{N_{tt}^2}{N_t}\frac{e_{td}}{i_{td}} + \frac{N_{tt}^2}{N_t}sL_{tt} + sL_{tl} \tag{19}$$

$$Z_{tqq} = \frac{N_{tt}^2}{N_t}\left(\frac{sL_t + R_t + G_{tcc}}{i_{td}G_{tcc}G_{tpll}}\right) + \frac{N_{tt}^2}{N_t}sL_{tt} + sL_{tl} \tag{20}$$

According to Equation (18), Z_{sdd} is equal to Z_{sqq}, because the HVDC sending terminal impedance does not contain coupling items and nonlinear parts such as PLL. Both Z_{sdd} and Z_{sqq} are independent of stable state points such as voltage and current. On the other hand, the inner current controller G_{scc}, outer AC voltage controller G_{sec} and LCL-filter parameters influence the HVDC impedance.

In contrast, according to Equations (19) and (20), the wind farm impedance Z_{sdd} and Z_{sqq} depend on stable state points such as e_{td}, i_{td} and v_{tdc}. Both Z_{tdd} and Z_{tqq} include the inner current controller G_{tcc} and L filter parameters. Moreover, the Z_{tdd} contains the DC voltage controller G_{tdc} because the DC voltage controller acts only on the *d-axes*, while Z_{tqq} has the PLL G_{tpll} for it acts only on the *q-axes*.

Figure 8 shows the Z_{dd} and Z_{qq} Nyquist plot of the HVDC and wind farm impedance interaction in increasing power ratios based on the system parameters in Table 1. Case I, Case II and Case III represent impedance based on a power ratio of 0.1 pu, 0.6 pu and 2 pu. For Z_{dd}, the three curves close in but are still far away from encircling the point (−1,j0), which means Z_{dd} is stable under these power ratios conditions. On the contrary, for Z_{qq}, the curves close in and finally in Case III the curve encircles the point (−1,j0) clockwise. Therefore, Z_{qq} is unstable under the highest power ratio. According to the GNC, the system is unstable if either Z_{dd} or Z_{qq} satisfies the instability criterion.

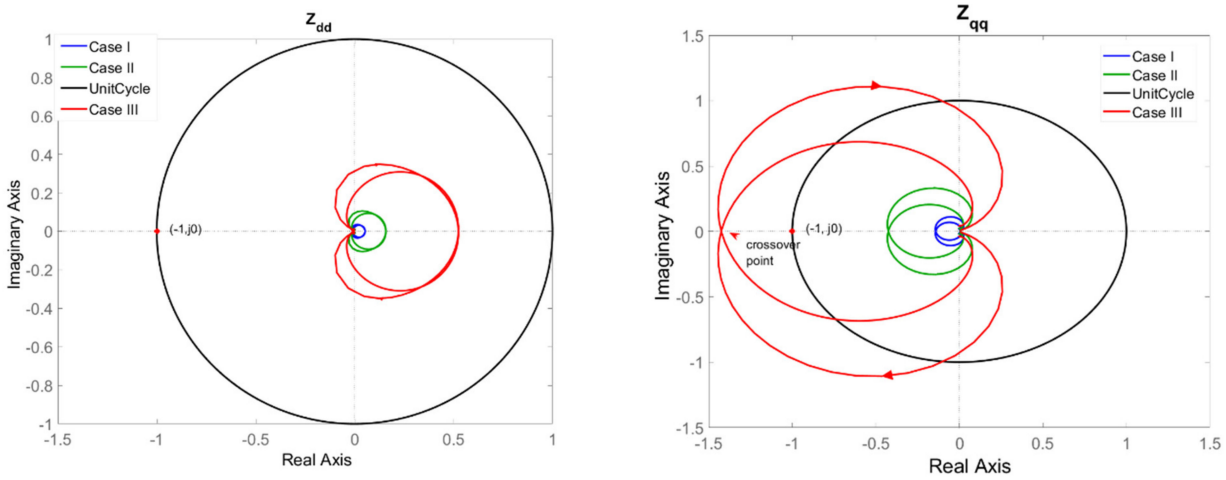

Figure 8. Nyquist plot of Z_{dd} and Z_{qq} with increasing power ratio.

Table 1. VSC-HVDC and equivalent wind farm system parameters.

Parameters	Value	Parameters	Value
Rated Power	100 MVA	L_t	0.2639 pu
Rated AC Voltage	160 kV	R_t	0.8402 pu
Rated Frequency	50 Hz	C_{tdc}	0.1486 pu
L_s	0.15 pu	v_{tdc}	1.929 pu
R_s	0.0039 pu	L_{tt}	0.0123 pu
C_s	6.217 pu		
L_{st}	0.057 pu		

Figure 9a shows the corresponding Bode plots, which show that as the active current i_{td} increases, the HVDC impedance $Z_{sdd,sqq}$ remains the same due to the independence of i_{td}. Meanwhile, the magnitude of wind farm impedance (Z_{tdd} and Z_{tqq}) decreases, as shown by the arrow. The Z_{tqq} in Case III reaches and crosses Z_{sqq} within 100 Hz. This tendency can be inferred by Equations (19) and (20), in which the active current i_{td} is the denominator of Z_{tdd} and Z_{tqq}.

The magnitude and phase change trends are demonstrated in the Bode plots of Z_{dd} and Z_{qq} in Figure 9b. The power ratios have small impact on the phases of Z_{dd} and Z_{qq}. The Z_{dd} phases cross at π on the frequency marked 'C'. The Z_{qq} magnitudes for Cases I and II have no crossover at 0 dB. Case III goes up to 0 dB at frequency A and then down to 0 dB on frequency B. If the frequency C is between A and B, Z_{qq} is unstable for Case III. This is the application of the Bode criterion, which corresponds to encircling the point (−1,j0) in Figure 8. On the other hand, the magnitudes of Z_{dd} have no crossover point, which demonstrates their stability.

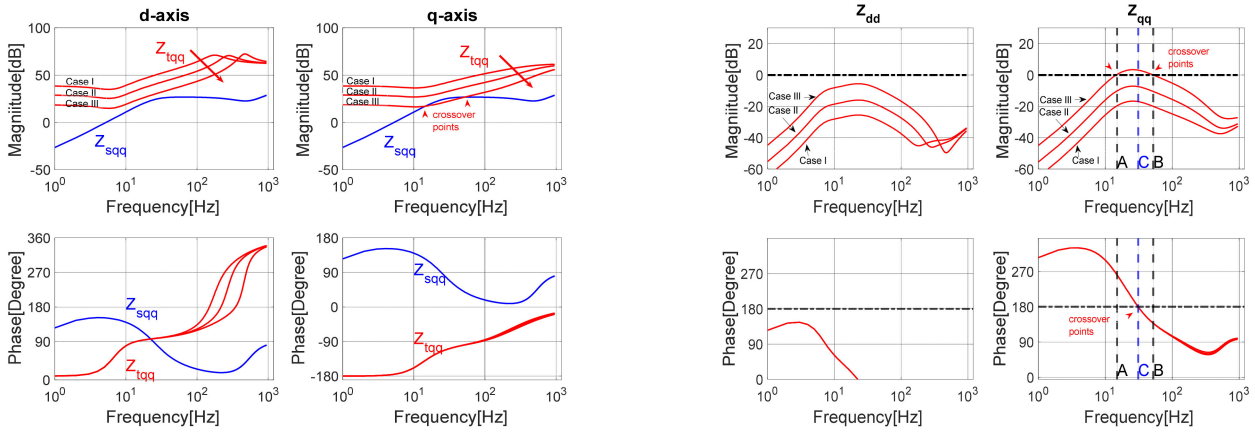

(**a**) (**b**)

Figure 9. System impedance interaction considering increased power ratio. (**a**) Bode plot of HVDC and wind farm impedance in *d* and *q*-axes. (**b**) Bode plot of Z_{dd} and Z_{qq} for system stability criterion.

The above discussion shows that the crossover points of magnitude are necessary for system instability, which is also the key reason for the sub/sup-SCI between the HVDC and wind farm system. To increase system stability, it is reasonable to avoid the crossover points by increasing the magnitudes of Z_{tdd} and Z_{tqq}, and decreasing those of Z_{sdd} and Z_{sqq} in the low range frequency.

Based on Equations (19) and (20), the number of grid-connected wind grid side converters N_t has an impact on the magnitude of wind farm impedance that is similar to that of the power ratio. It is obvious that the worst-case scenario occurs when the whole wind farm delivers its rated power. The following analysis will be based on this extreme condition.

3.3. Impact of Line Impedance on System Stability

To analyze the line impedance impact on the system stability, Z_{tdd} and Z_{tqq} are studied without line impedance and with 100 mH line impedance.

The HVDC and wind farm impedance interactions without and with line impedance are shown in Figure 10a. The phase part of Z_{tdd} shows that it is a positive resistive-inductive load for very low frequency range (between 0 Hz and about 30 Hz), as the phase is between 0 and 90 degrees. Between 30 Hz and about 310 Hz, the Z_{tdd} impedance is a negative resistive-inductive load, when its phase is between $\pi/2$ and π. This is the main phase characteristic of Z_{tdd} in the frequency domain.

As the inductive line impedance is added, the magnitudes of Z_{tdd} increase for frequencies between 0 Hz and around 310 Hz, as shown in Figure 10a. This increases the magnitude difference between the HVDC and wind farm on the *d-axes* and eliminates the possibilities of crossover. Based on the previous system stability analysis, the increased line impedance decreased the risk of Z_{tdd} instability.

On the contrary, the Z_{tqq} impedance has a negative resistive-capacitive load when the frequency is between 0 Hz and around 30 Hz, with its phase between $-\pi$ and $-\pi/2$. The impedance turns to a positive resistive-capacitive load for frequencies between 30 Hz and more than 100 Hz. Consequently, the amplitude of Z_{tqq} decreases with the added line inductance impedance. This increased the possibility of HVDC and wind farm magnitude crossover points. Based on the previous system stability analysis, it can be stated that the line impedance increases the risk of Z_{tqq} instability. As the Bode plots of interactions in the *q-axes* show, with the 100 mH line impedance, the magnitude of wind farm has crossover points with the HVDC magnitude, which will lead to system stability.

Figure 10b shows the Bode plots of Z_{dd} and Z_{qq} considering line impedance. Z_{dd} magnitudes do not have crossover points with the 0 dB line, which indicates their stability. Meanwhile, the line impedance causes crossover points for Z_{qq} magnitude with 0 dB. With

the phase conditions and based on the Bode criterion mentioned previously, Z_{qq} with line impedance is unstable. This proves theoretically that a certain line impedance can cause system instability.

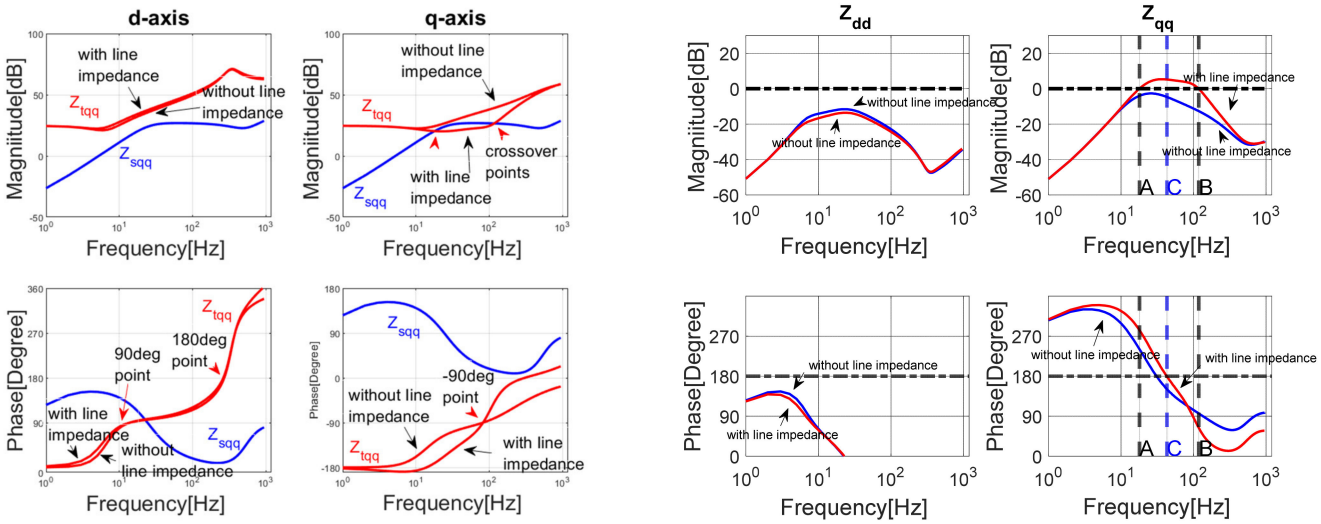

(**a**) (**b**)

Figure 10. System impedance interaction considering line impedance. (**a**) Bode plot of HVDC and wind farm impedance on the *dq*-axis. (**b**) Bode plots of Z_{dd} and Z_{qq} for system stability criterion.

3.4. Impact of Control Loop Bandwidths on Stability

According to the previous interpretation, the impedance models contain PI controllers, which are designed by considering control loop bandwidth and the damping ratio (set to 0.707). Therefore, it is more reasonable to investigate the relationship between system stability and control loop bandwidths, rather than the individual proportional or integral coefficients.

The controllers can be redefined as follows, by replacing the proportional and integral coefficients by their bandwidth for each PI controller in Equations (3)–(5), and (7)–(14) where the defined damping ratios are equal to 0.707.

$$G_{scc} = \omega_{scc}\left(L_s + \frac{R_s}{s}\right),\ G_{sec} = \omega_{sec}\left(0.6857C_s + \omega_{\mathrm{sec}}\frac{0.236C_s}{s}\right)$$

$$G_{tcc} = \omega_{tcc}\left(L_t + \frac{R_t}{s}\right),\ G_{tdcc} = \omega_{tdcc}\left(0.6857C_{tdc} + \omega_{tdcc}\frac{0.236C_{tdc}}{s}\right)$$

$$G_{tpll} = \frac{1}{e_{td}}\frac{\left(0.6857\omega_{tpll}s + 0.236\omega_{tdcc}^2\right)}{s^2 + 0.6857\omega_{tpll}s + 0.236\omega_{tdcc}^2}$$

It is more specific to study the impact of bandwidth on stability by inserting these controllers into Equations (18)–(20) and obtaining Equations (21)–(23) below:

$$Z_{sdd,sqq} = N_{st}^2\frac{\omega_{scc}\omega_{sec}\left(0.6857 + \omega_{\mathrm{sec}}\frac{0.236}{s}\right) + (s\omega_{scc} + 1)}{sC_s\left(\omega_{scc}\omega_{sec}\left(0.6857 + \omega_{\mathrm{sec}}\frac{0.236}{s}\right) + (s\omega_{scc} + 1)\right)^2 + (\omega C_s)^2} + sL_{st} \tag{21}$$

$$Z_{tdd} = \frac{N_{tt}^2}{N_t}\left(\frac{\frac{s}{\omega_{tcc}} + 1}{\left(0.6857 + \omega_{tdcc}\frac{0.236}{s}\right)}\right)\frac{sv_{tdc}}{i_{td}} - \frac{N_{tt}^2}{N_t}\frac{e_{td}}{i_{td}} + \frac{N_{tt}^2}{N_t}sL_{tt} + sL_{tl} \tag{22}$$

$$Z_{tqq} = \frac{N_{tt}^2}{N_t}\left(\frac{\frac{s}{\omega_{tcc}}+1}{\frac{0.6857\omega_{tpll}s+0.236\omega_{tdcc}^2}{s^2+0.6857\omega_{tpll}s+0.236\omega_{tdcc}^2}}\right)\frac{e_{td}}{i_{td}} + \frac{N_{tt}^2}{N_t}sL_{tt} + sL_{tl} \quad (23)$$

3.4.1. Impact of HVDC Controller Loop Bandwidths

Due to the inner and outer control loops design principle, the bandwidth of the inner current control loop should be set as 10 times that of the outer AC voltage control loop. Therefore, it is logical to keep the relationship between the two bandwidths fixed when discussing the impact of bandwidths on impedance.

From Equation (21), it is clear that the highest orders of the current control loop bandwidth ω_{scc} and the AC voltage control loop bandwidth ω_{sec} in the denominator are two and four, respectively, which are double those in their respective numerators. This signifies that the reduction in ω_{scc} and ω_{sec} will increase Bode plots magnitudes, which raises the stability risk.

Figure 11a shows the Z_{tdd} and Z_{tqq} Bode plots under different bandwidths in proportional change. In the presence of the wind farm impedance, the current bandwidth is reduced from 10 pu (500 Hz) (Case I) to 9 pu (450 Hz) (Case II), while the outer AC voltage control loop bandwidth is reduced from 1 pu (50 Hz) (Case I) to 0.9 pu (45 Hz) (Case II), and the magnitude of Z_{tqq} rose and crosses the wind farm impedance.

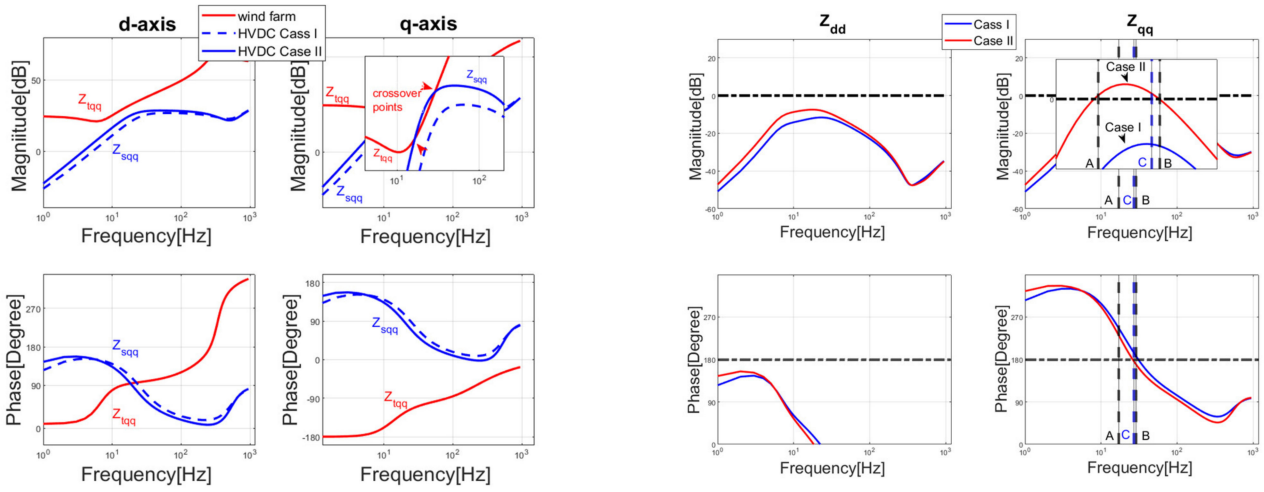

(**a**) (**b**)

Figure 11. System impedance interaction considering reduced HVDC control loop bandwidths. (**a**) Bode plots of HVDC and wind farm impedance on the *dq*-axis. (**b**) Bode plots of Z_{dd} and Z_{qq} for system stability criterion.

In Figure 11b, the Bode plots of Z_{dd} and Z_{qq} can show this variation from a stable to unstable condition. The magnitude of Case I in the *q-axes* has no crossover points with the 0 dB line. The magnitude of Case II in the *q-axes* has a crossover up to the 0 dB line before its phase crosses down to the π line, and subsequently crosses back down to 0 dB after the phase crosses down to π. This indicates that Z_{qq} changes from stable to unstable when the bandwidths change. Although the magnitude of Z_{dd} also increases, it is too small and the phase of Z_{dd} will not affect the system stability.

3.4.2. Impact of Wind Grid Side Controller Loop Bandwidths

According to Z_{tdd} in Equation (22), ω_{tdcc} exists only in the denominator. Therefore, the bandwidths and Z_{tdd} magnitude are inversely proportional. It can be observed from Equations (22) and (23), that ω_{tcc} exists in the form of s/ω_{tcc} + 1 the in numerators of both equations. Due to its relatively higher value compared to 1, ω_{tcc} has a small impact on the magnitudes of Z_{tdd} and Z_{tqq}.

Figure 12 compares Z_{tdd} and Z_{tqq} for different values of ω_{tcc} and ω_{tdcc}. Firstly, only ω_{tcc} increases from 4 pu (200 Hz) (Case I) to 8 pu (400 Hz) (Case II), while the ω_{tdcc} is fixed at 0.8 pu (40 Hz). These two cases show little impact on either Z_{tdd} or Z_{tqq} in magnitude or phase. Secondly, in Case III, ω_{tdcc} changes from 0.4 pu (20 Hz) (Case I) up to 0.8 pu (40 Hz), while ω_{tcc} is kept fixed at 4 pu (200 Hz). The magnitude of Z_{tdd} decreases while that of Z_{tqq} remains stable. The lowest magnitude points of Z_{tdd} move closer to those of Z_{sdd}, which indicates the rising risk of instability, but considering the phase conditions, it is hard for Z_{tdd} to lead to system instability.

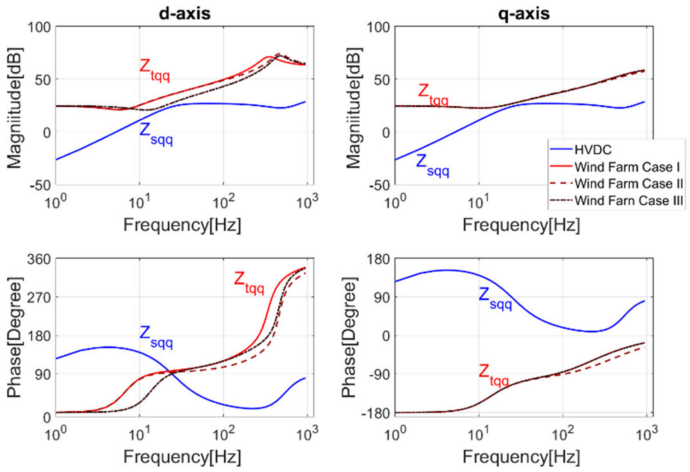

Figure 12. System impedance interaction considering reduced wind converter control loop bandwidth.

It can be observed from Equation (23) that the ω_{tpll} is part of Z_{tqq} denominator in a form of second-order function. Therefore, when the ω_{tpll} increases, the Z_{tqq} magnitude in the increased bandwidth area will decrease rapidly and rest frequency areas almost remain the same.

Figure 13a shows the Z_{tqq} with ω_{tpll} from 20 Hz (Case I) to 50 Hz (Case II). The magnitude falls to have crossover with Z_{sqq}. The range of phase near $-\pi$ are extended from 4 to 12 Hz, which increased the possibility of phase instability. However, because ω_{tpll} has no impacts on Z_{sdd} as mentioned before, Z_{sdd} remains the same.

Figure 13b is the Bode plot of Z_{qq} and shows that Z_{qq} becomes unstable from an originally stable condition.

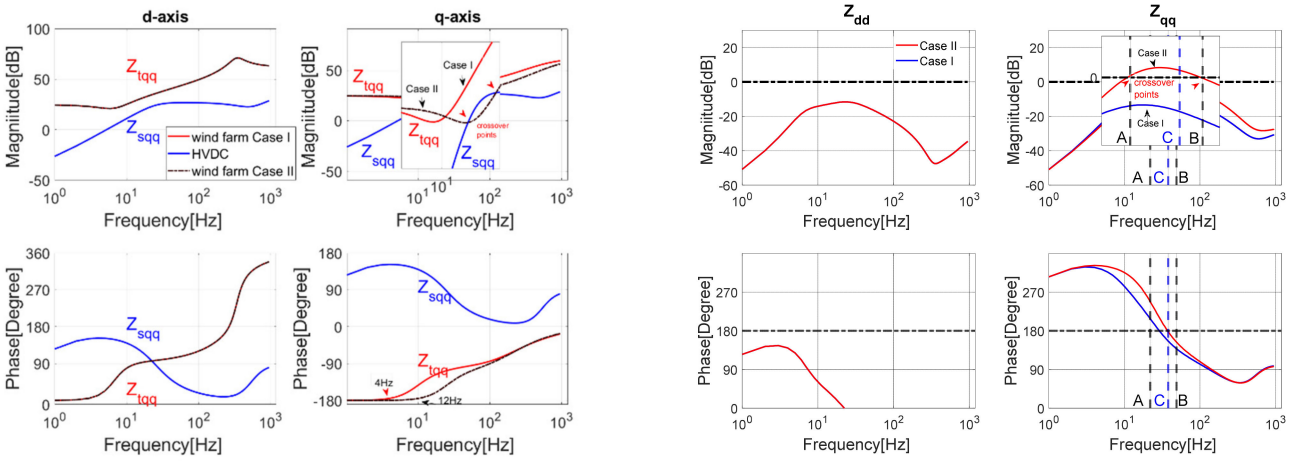

(**a**) (**b**)

Figure 13. System impedance interaction considering increased wind converter PLL bandwidths. (**a**) Bode plot of HVDC and wind farm impedance on the *dq*-axis. (**b**) Bode plots of Z_{dd} and Z_{qq} for system stability criterion.

3.5. Impacts of Wind Grid Side Converter Switching Frequency

Considering the switching losses and limitations of the switching devices, the switching frequency for a wind power converter is in the range of 1–2 kHz. This limits its bandwidths, such as ω_{dcc}, ω_{tcc}, and ω_{tpll}. Developments in power switching devices, such as SiC and the multilevel topology application, have enabled the wind grid side converters to have a higher switching frequency, such as 3 kHz and more. Consequently, wider bandwidths are allowed, especially for ω_{tpll}. Therefore, the higher switching frequency may have the same impact on system stability as the increased ω_{tpll}.

4. Simulation Results and Stability Improvement by Bandwidth Modification

In this section, case studies will be presented to verify the previous conclusions by Matlab/Simulation. Subsequently, stability improvements by means of modifying the bandwidths will be proposed. Table 2 shows the VSC-HVDC and equivalent wind farm control bandwidths for a stable system.

Table 2. VSC-HVDC and equivalent wind farm system control bandwidths.

Parameters	Value	Parameters	Value
ω_{scc}	7 pu	ω_{tcc}	6 pu
ω_{sec}	0.7 pu	ω_{tdcc}	0.6 pu
		ω_{tpll}	0.9 pu

Figure 14 shows the PCC phase voltage and current in the *abc*-frame under free line impedance, and Table 3 shows their FFT spectra. This figure and table show that the system only contains voltage and current at a frequency of 50 Hz. Therefore, the system operates in a stable condition.

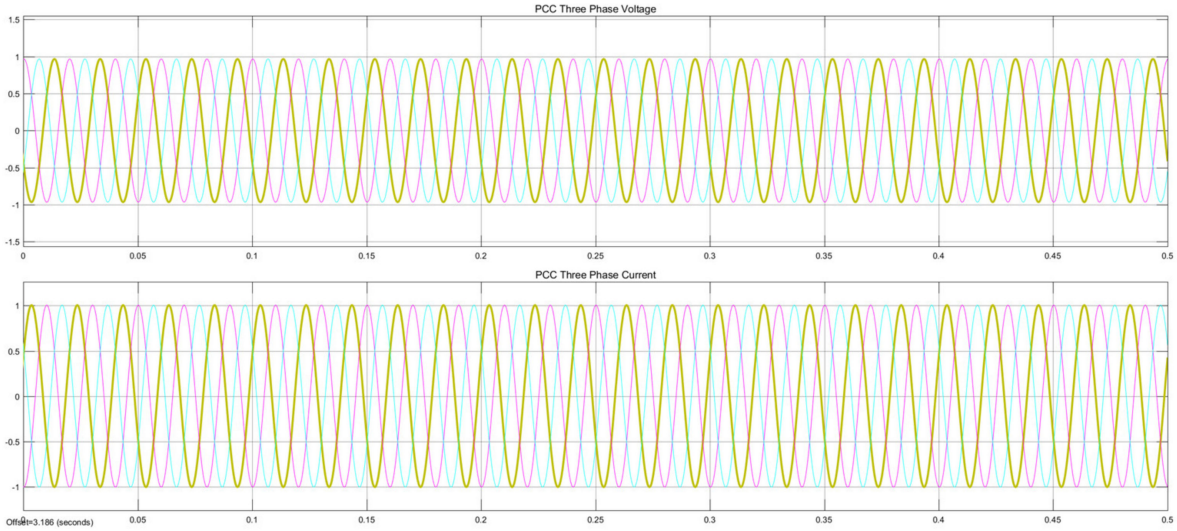

Figure 14. PCC three phase instantaneous voltage and current (pu) in stable condition.

Table 3. FFT spectra of PCC voltage and current under stable condition.

	PCC Voltage	Value (50 Hz Based pu)	PCC Current	Value (50 Hz Based pu)
FFT Spectrum	50 Hz (based frequency)	1	50 Hz (based frequency)	1

4.1. Simulations on the Line Impedance Impact

Figure 15a shows the Bode plots of Z_{dd} and Z_{qq} when the line impedance is 100 mH. The plot of Z_{qq} shows that the system becomes unstable. Figure 15b shows the PCC instantaneous voltage and current, and Table 4 shows their FFT spectra. Both the voltages and currents have low frequency oscillations at around 8 Hz, 108 Hz, 21 Hz and 79 Hz. This proves that line impedance can lead to system instability.

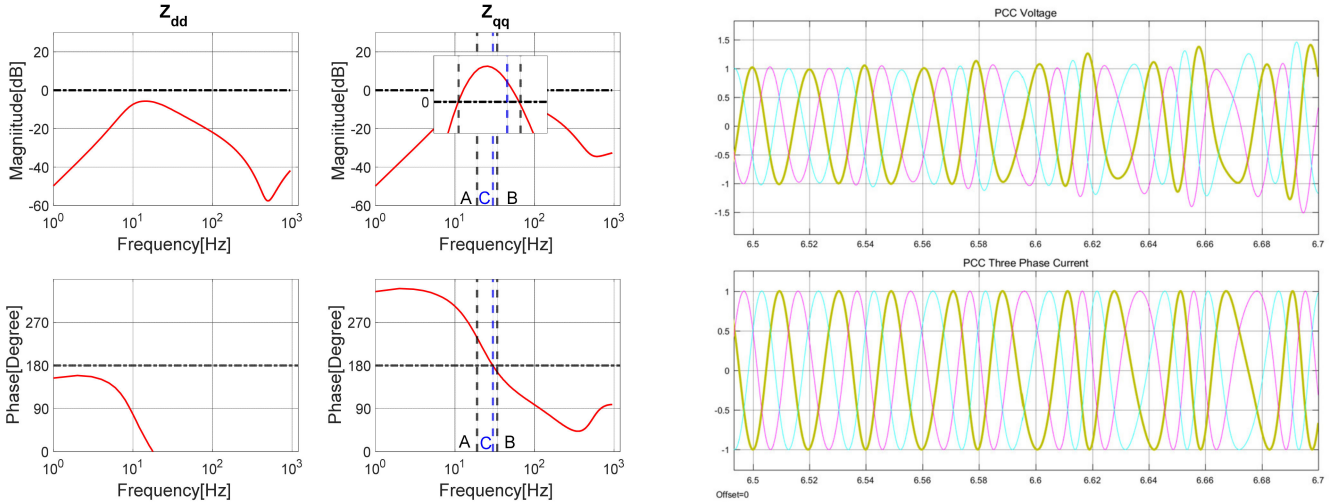

(**a**) (**b**)

Figure 15. Unstable conditions by line impedance. (**a**) Bode plots of Z_{dd} and Z_{qq} for system instability criterion. (**b**) Instantaneous PCC voltage and current (pu).

Table 4. FFT spectra of voltage and current under unstable conditions caused by line impedance.

	PCC Voltage	Value (50 Hz Based pu)	PCC Current	Value (50 Hz Based pu)
FFT Spectrum	50 Hz (base frequency)	1	50 Hz (base frequency)	1
	8 Hz	0.05	8 Hz	0.07
	21 Hz	0.22	21 Hz	0.35
	79 Hz	0.43	79 Hz	0.36
	108 Hz	0.05	108 Hz	0.04

4.2. Simulation on the Bandwidths Impact

Figure 16a shows the Bode plots of Z_{dd} and Z_{qq} where ω_{scc} and ω_{sec} are 6 pu (300 Hz) and 0.6 pu (30 Hz), respectively, which are reduced from the original 7 pu (350 Hz) and 0.7 pu (35 Hz), respectively. It shows that the system becomes unstable in Z_{qq}. The unstable simulation results of the three phases' voltage and current and their FFT spectra are provided in Figure 16b and Table 5, respectively. The table shows that the oscillation frequency is around 24.5 and 75.5 Hz, respectively. Compared with the three phases' voltage and current in Figure 14, the reductions in ω_{scc} and ω_{sec} are the reasons for this system instability.

Figure 17a shows the Bode plots of Z_{dd} and Z_{qq} when the ω_{tpll} changes from 45 Hz to 68 Hz. The Z_{qq} is unstable according to the Bode criterion. Figure 17b shows its three-phase voltage and current, in which the oscillation occurs. Table 6 shows that the voltage and current oscillation frequencies are about 15 Hz and 85 Hz. The increased ω_{tpll} could cause the system to become unstable.

To validate the previous analysis about the inner current and outer DC voltage control loop bandwidth impact, simulations that double the bandwidths ω_{tcc} and ω_{tdcc} from the original 300 Hz and 30 Hz to 600 Hz and 60 Hz were carried out. The system is still stable,

the three-phase voltage and current similar to those in Figure 14. This shows these two bandwidths have little impact on system stability as indicated by the previous study.

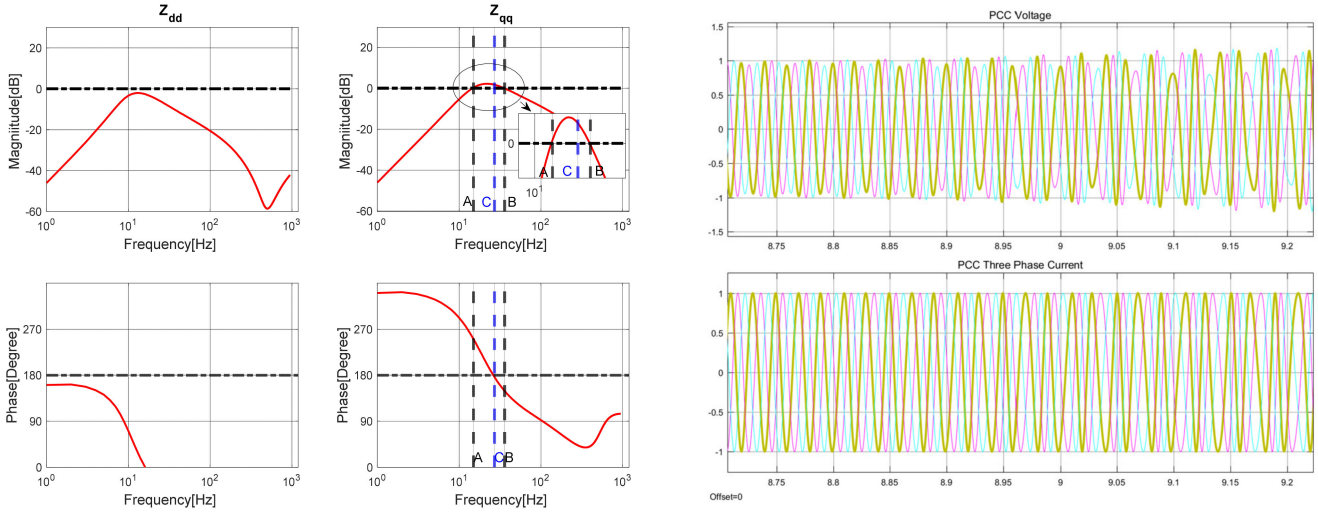

(**a**) (**b**)

Figure 16. System instability conditions caused by decreasing HVDC bandwidths. (**a**) Bode plots of Z_{dd} and Z_{qq} for system. (**b**) Instantaneous PCC voltage and current (pu).

Table 5. FFT spectra of voltage and current under unstable conditions caused by decreased HVDC bandwidths.

	PCC Voltage	Value (50 Hz Based pu)	PCC Current	Value (50 Hz Based pu)
FFT Spectrum	50 Hz (base frequency)	1	50 Hz (base frequency)	1
	1 Hz	0.12	1 Hz	0.18
	24.5 Hz	0.40	24.5 Hz	0.58
	75.5 Hz	0.55	75.5 Hz	0.59
	101 Hz	0.11	101 Hz	0.17

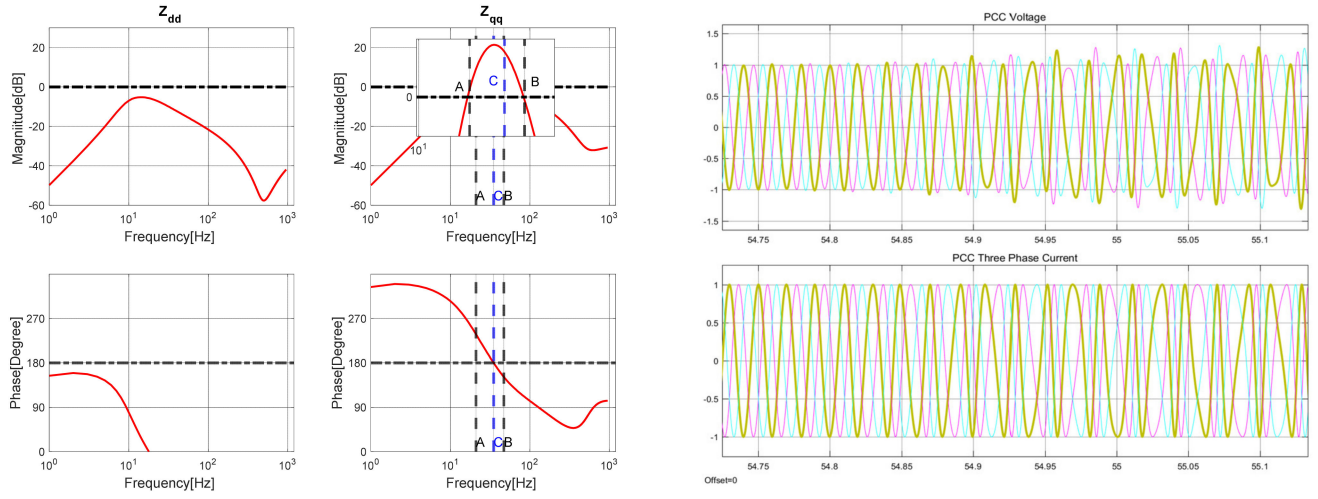

(**a**) (**b**)

Figure 17. Unstable system caused increased wind farm PLL bandwidth. (**a**) Bode plots of Z_{dd} and Z_{qq}. (**b**) Instantaneous PCC voltage and current (pu).

Table 6. FFT spectra of voltage and current under unstable conditions caused by increased wind farm PLL bandwidth.

	PCC Voltage	Value (50 Hz Based pu)	PCC Current	Value (50 Hz Based pu)
FFT Spectrum	50 Hz (based frequency)	1	50 Hz (based frequency)	1
	15 Hz	0.29	15 Hz	0.44
	85 Hz	0.38	85 Hz	0.43

4.3. Stability Improvement by Bandwidth Modification

The simulations shown earlier serve as proof of the previous theoretical study. Based on this, there are two ways to improve the system stability by bandwidth modification: (1) reduce the ω_{tpll} of wind grid side converters; (2) enlarge the HVDC bandwidths.

The following simulations compare two methods of system stability improvement by bandwidth modification. Figure 18 shows the Bode plots of Z_{dd} and Z_{qq} for three cases. Case I is the unstable system, which is the same as that shown in Figure 14 with 150 mH line impedance. Case II reduces the ω_{tpll} from the original 0.9 pu (45 Hz) to 0.4 pu (20 Hz), while Case III extends the ω_{scc} and ω_{sec} from the original 7 pu (350 Hz) and 0.7 pu (35 Hz) to 10.7 pu (535 Hz) and 1.07 pu (53.5 Hz).

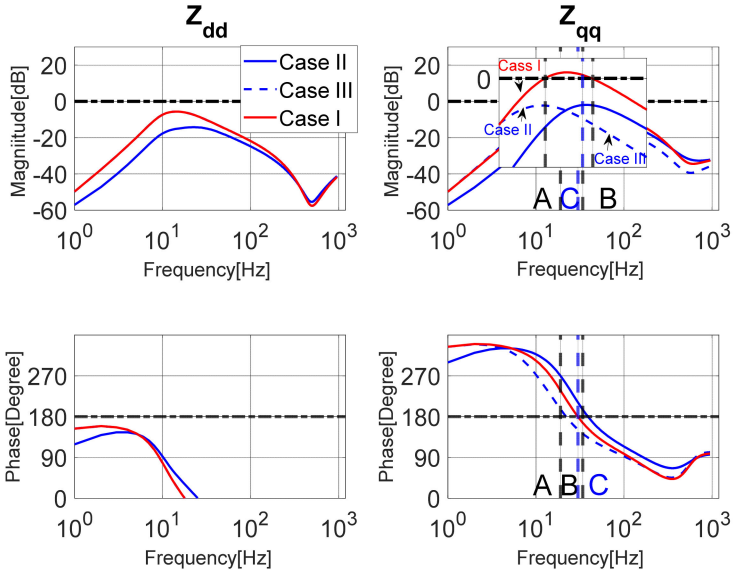

Figure 18. System stability improvement by wind farm bandwidths and HVDC bandwidths.

The magnitude of Z_{qq} in Case I has crossover points with 0 dB, which is the key condition causing instability. Previous simulation has ready shown its unstable result. Both Cases II and III reduce the magnitude of Z_{qq}, which avoids the crossover points. In Cases II and III the system become stable by the Bode criterion. Simulations validate the impact of bandwidth modification methods.

Based on the observation that in Cases II and III that the magnitude reaches Z_{qq} the same level, it can be gathered that the changes in ω_{scc}, ω_{sec} and ω_{tpll} have an equivalent function. Therefore, the relationship between ω_{scc}, ω_{sec} and ω_{tpll} can be found to have a similar impact on Z_{qq} magnitude within a certain range. In Figure 19, the original point is (45, 35), which means ω_{tpll} = 45 Hz and ω_{sec} = 0.1ω_{see} = 35 Hz. The point (40, 36.7) in the curve in Figure 19 signified that a 5 Hz reduction in ω_{tpll} and a 1.7 Hz increment in ω_{sec} (a 17 Hz increment of ω_{scc}) can reduce the Z_{qq} magnitude to the same degree. Based on this figure, it can be concluded that generally the Z_{qq} magnitude is more sensitive to ω_{sec} (ω_{scc}) than ω_{tpll} within certain a bandwidth range.

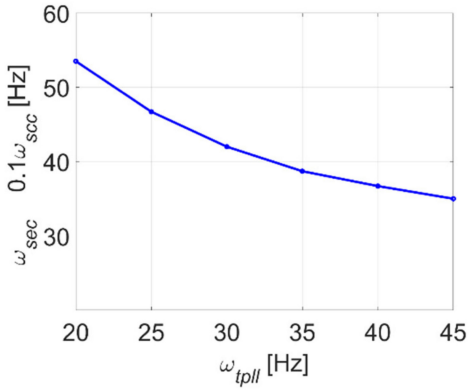

Figure 19. Equivalent relationship between wind farm PLL bandwidth and HVDC bandwidths.

However, the LVRT and HVRT require the wind grid side converters to have a fast response, which needs the ω_{tpll} to be set to a high value. Meanwhile, the HVDC needs to limit its bandwidths to take into consideration the possible disturbance. Consequently, the ability to enhance the system stability by bandwidth modification is effective but has limited utility.

By techno-economic and risk analysis (TERA), bandwidths' modification to enhance the system stability is an economical method compared with using oscillation suppression devices. The economic losses in sub/sup-synchronous interaction events are also significant. Between only September 2015 and September 2016, there were over 111 cases recorded in China. Each time the lost wind power was at least 50 MW; sometimes it could be up to 300 MW. The approved sub/sup-synchronous interaction depression method application is expected to avoid these losses with minor expense.

5. Discussion and Conclusions

This paper presented an analysis of sub/super-SCI in a VSC-HVDC and PMSG-based wind farm system with AC transmission line. After simplifying the impedance equations, a Bode criterion for system stability was used, which showed the unstable magnitude and phase conditions more clearly than the GNC. The wind farm impedance phase on the *q-axes* easily satisfied the instability condition due to the negative resistive-capacitive chrematistics. Therefore, the *q-axes* magnitude crossover points between the wind farm and HVDC were essential for system stability. The mathematical relations between the impedance magnitude and elements were demonstrated explicitly according to the detailed impedance expression. The results suggested that increasing the power ratio and line impedance helped form the crossover point by reducing the wind farm *q-axes* impedance magnitude. It was also discovered that the reduction in the HVDC and extension of the wind farm PLL control loop bandwidths affected the system stability in a similar manner. The outer DC voltage control loop bandwidth and inner current control loop of the wind converters had a negligible impact on *q-axes* magnitude and phase.

It is possible to improve system stability by reducing the PLL bandwidth and extending the bandwidths of HVDC, and simulation results supported this analysis. However, the limitations of this improvement approach were also discussed. It was found that the magnitude was more sensitive to HVDC bandwidth than that of the PLL; therefore, it was better to modify the HVDC bandwidth. Thus, the stability was optimized to a certain degree by bandwidth adjustments.

Compared with the oscillation suppression device installations, the approach this paper provided, which offered guidance to redesign the relevant controllers' bandwidths, was easy to access in application in a low-cost way. However, this method only increased the magnitude margin of Z_{qq}. The unstable phase condition of Z_{qq} was hard to change. As a consequence, accurate parameters for impedance models were required and robustness of this approach was reduced.

Author Contributions: Conceptualization, X.T. and C.W.; methodology, Y.Z. and H.C.; software, Y.Z.; validation, X.T. and H.C.; writing—original draft preparation, Y.Z.; writing—review and editing, Y.Z., X.T. and H.C. All authors have read and agreed to the published version of the manuscript.

Funding: This research was funded by the National Natural Science Foundation of China under Grant No. 51577187 and the Fundamental Research Funds for the Central Universities grant number 2021YJSJD15.

Data Availability Statement: All data used in this research is available upon requirement.

Conflicts of Interest: The authors declare on conflict of interest.

References

1. Mahela, O.P.; Gupta, N.; Khosravy, M.; Patel, N. Comprehensive Overview of Low Voltage Ride through Methods of Grid Integrated Wind Generator. *IEEE Access* **2019**, *7*, 99299–99326. [CrossRef]
2. Dos Santos, M.L.; Jardini, J.A.; Casolari, R.P.; Vasquez-Arnez, R.L.; Saiki, G.Y.; Sousa, T.; Nicola, G.L.C. Power Transmission Over Long Distances: Economic Comparison Between HVDC and Half-Wavelength Line. *IEEE Trans. Power Deliv.* **2014**, *29*, 502–509. [CrossRef]
3. Li, R.; Yu, L.; Xu, L.; Adam, G.P. Coordinated Control of Parallel DR-HVDC and MMC-HVDC Systems for Offshore Wind Energy Transmission. *IEEE J. Emerg. Sel. Top. Power Electron.* **2020**, *8*, 2572–2582. [CrossRef]
4. Flourentzou, N.; Agelidis, V.G.; Demetriades, G.D. VSC-Based HVDC Power Transmission Systems: An Overview. *IEEE Trans. Power Electron.* **2009**, *24*, 592–602. [CrossRef]
5. Wang, Y.; Zhao, C.; Guo, C.; Rehman, A.U. Dynamics and Small Signal Stability Analysis of PMSG-Based Wind Farm with an MMC-HVDC System. *CSEE J. Power Energy Syst.* **2020**, *6*, 226–235.
6. Wang, Y.; Wang, L.; Jiang, Q. Impact of Synchronous Condenser on Sub/Super-Synchronous Oscillations in Wind Farms. *IEEE Trans. Power Deliv.* **2020**, *36*, 2075–2084. [CrossRef]
7. Ebrahimzadeh, E.; Blaabjerg, F.; Wang, X.; Bak, C.L. Reducing Harmonic Instability and Resonance Problems in PMSG-Based Wind Farms. *IEEE J. Emerg. Sel. Top. Power Electron.* **2018**, *6*, 73–83. [CrossRef]
8. Adams, J.; Carter, C.; Huang, S.-H. ERCOT Experience with sub-synchronous control interaction and proposed remediation. In Proceedings of the PES T D 2012, Orlando, FL, USA, 7–10 May 2012; pp. 1–5.
9. Wang, L.; Xie, X.; Jiang, Q.; Liu, H.; Li, Y.; Liu, H. Investigation of SSR in Practical DFIG-Based Wind Farms Connected to a Series-Compensated Power System. *IEEE Trans. Power Syst.* **2015**, *30*, 2772–2779. [CrossRef]
10. Sun, K.; Yao, W.; Fang, J.; Ai, X.; Wen, J.; Cheng, S. Impedance Modeling and Stability Analysis of Grid-Connected DFIG-Based Wind Farm With a VSC-HVDC. *IEEE J. Emerg. Sel. Top. Power Electron.* **2020**, *8*, 1375–1390. [CrossRef]
11. Zhu, L.; Zhong, D.; Wang, B.; Lin, R.; Xu, M. Understanding Subsynchronous Oscillation in DFIG-Based Wind Farms with Rotor-Side Converter Control Based on the Equivalent RLC Model. *IEEE Access* **2020**, *8*, 65371–65382. [CrossRef]
12. Lv, J.; Dong, P.; Shi, G.; Cai, X.; Rao, H.; Chen, J. Subsynchronous oscillation of large DFIG-based wind farms integration through MMC-Based HVDC. In Proceedings of the 2014 International Conference on Power System Technology, Chengdu, China, 20–22 October 2014; pp. 2401–2408.
13. Lv, J.; Dong, P.; Shi, G.; Cai, X.; Li, X. Subsynchronous Oscillation and Its Mitigation of MMC-Based HVDC with Large Doubly-Fed Induction Generator-Based Wind Farm Integration. *Proc. CSEE* **2015**, *35*, 4852–4860.
14. Hanchao, L.; Jian, S. Voltage Stability and Control of Offshore Wind Farms with AC Collection and HVDC Transmission. *IEEE J. Emerg. Sel. Top. Power Electron.* **2014**, *2*, 1181–1189. [CrossRef]
15. Sowa, I.; Domínguez-García, J.L.; Gomis-Bellmunt, O. Impedance-Based Analysis of Harmonic Resonances in HVDC Connected Offshore Wind Power Plants. *Electr. Power Syst. Res.* **2019**, *166*, 61–72. [CrossRef]
16. Lv, J.; Cai, X.; Zhang, Z.; Chi, Y. Impedance Modeling and Stability Analysis of MMC-based HVDC for Offshore Wind Farms. *Proc. CSEE* **2016**, *36*, 3771–3781.
17. Amin, M.; Molinas, M. Understanding the Origin of Oscillatory Phenomena Observed Between Wind Farms and HVdc Systems. *IEEE J. Emerg. Sel. Top. Power Electron.* **2017**, *5*, 378–392. [CrossRef]
18. Xie, X.; Liu, H.; He, J.; Zhang, C.; Qiao, Y. Mechanism and Characteristics of Subsynchronous Oscillation Caused by the Interaction between Full-converter Wind Turbines and AC Systems. *Proc. CSEE* **2016**, *36*, 2366–2372.
19. Lv, J.; Cai, X. Controller Parameters Optimization Design for Enhancing the Stability of Wind Farm With VSC-HVDC System. *Proc. CSEE* **2018**, *38*, 431–434.
20. Amin, M.; Molinas, M.; Lyu, J. Oscillatory phenomena between wind farms and HVDC systems: The impact of control. In Proceedings of the 2015 IEEE 16th Workshop on Control and Modeling for Power Electronics (COMPEL), Vancouver, BC, Canada, 12–15 July 2015; pp. 1–8.
21. Lyu, J.; Cai, X.; Amin, M.; Molinas, M. Sub-synchronous Oscillation Mechanism and Its Suppression in MMC-based HVDC Connected Wind Farms. *IET Gener. Transm. Amp Distrib.* **2018**, *12*, 1021–1029. [CrossRef]

22. Qoria, T.; Gruson, F.; Colas, F.; Guillaud, X.; Debry, M.-S.; Prevost, T. Tuning of cascaded controllers for robust grid-forming voltage source converter. In Proceedings of the 2018 Power Systems Computation Conference (PSCC), Dublin, Ireland, 11–15 June 2018; pp. 1–7.
23. Wang, X.; Harnefors, L.; Blaabjerg, F. Unified Impedance Model of Grid-Connected Voltage-Source Converters. *IEEE Trans. Power Electron.* **2018**, *33*, 1775–1787. [CrossRef]
24. Wen, B.; Boroyevich, D.; Burgos, R.; Mattavelli, P.; Shen, Z. Analysis of D-Q Small-Signal Impedance of Grid-Tied Inverters. *IEEE Trans. Power Electron.* **2016**, *31*, 675–687. [CrossRef]
25. Harnefors, L. Modeling of Three-Phase Dynamic Systems Using Complex Transfer Functions and Transfer Matrices. *IEEE Trans. Ind. Electron.* **2007**, *54*, 2239–2248. [CrossRef]
26. Burgos, R.; Boroyevich, D.; Wang, F.; Karimi, K.; Francis, G. On the Ac stability of high power factor three-phase rectifiers. In Proceedings of the 2010 IEEE Energy Conversion Congress and Exposition, Atlanta, GA, USA, 12–16 September 2010; pp. 2047–2054.
27. Wen, B.; Boroyevich, D.; Burgos, R.; Mattavelli, P.; Shen, Z. Inverse Nyquist Stability Criterion for Grid-Tied Inverters. *IEEE Trans. Power Electron.* **2017**, *32*, 1548–1556. [CrossRef]
28. Fan, L.; Miao, Z. Admittance-Based Stability Analysis: Bode Plots, Nyquist Diagrams or Eigenvalue Analysis? *IEEE Trans. Power Syst.* **2020**, *35*, 3312–3315. [CrossRef]